JACS
JOURNAL OF THE AMERICAN CHEMICAL SOCIETY
pubs.acs.org/JACS
Article

Dicarboxylic Acids Induced Tandem Transformation of Silver Nanocluster

Zhi Wang, Rakesh Kumar Gupta, Fahri Alkan, Bao-Liang Han, Lei Feng, Xian-Qiang Huang, Zhi-Yong Gao, Chen-Ho Tung, and Di Sun*

Cite This: J. Am. Chem. Soc. 2023, 145, 19523−19532
Read Online
ACCESS | Metrics & More | Article Recommendations | Supporting Information

ABSTRACT: Structural transformation of metal nanoclusters (NCs) is of great ongoing interest regarding their synthesis, stability, and reactivity. Although sporadic examples of cluster transformations have been reported, neither the underlying transformation mechanism nor the intermediates are unambiguous. Herein, we have synthesized a flexible 54-nuclei silver cluster (**Ag54**) by combining soft (^{t}BuC≡C$^-$) and hard (^{n}PrCOO$^-$) ligands. The existence of weakly coordinated ^{n}PrCOO$^-$ enhances the reactivity of **Ag54**, thus facilitating the dicarboxylic acid to induce structural transformation. X-ray structural analyses reveal that **Ag54** transforms to Ag_{28} cluster-based 2D networks (**Ag28a** and **Ag28b**) induced by H_2suc (succinic acid) and H_2glu (glutaric acid), whereas with H_2pda (2,2′-(1,2-phenylene)diacetic acid), a discrete Ag_{28} cluster (**Ag28c**) is isolated. The key intermediate **Ag17** that emerges during the self-dissociation of **Ag54** was isolated by using cryogenic recrystallization and characterized by X-ray crystallography. The "tandem transformation" mechanism for the structure evolution from **Ag54** to **Ag28a** is established by time-dependent electrospray ionization mass spectrometry (ESI-MS) and UV−vis spectroscopy. In addition, the catalytic activity in the 4-nitrophenol reduction follows the sequence **Ag28c** > **Ag28b** > **Ag28a** > **Ag54** due to more bare silver sites on the surface of the Ag_{28} cluster unit. Our findings not only open new avenues to the synthesis of silver NCs but also shed light on a better understanding of the structural transformation mechanism from one cluster to another or cluster-based metal−organic networks induced by dicarboxylates.

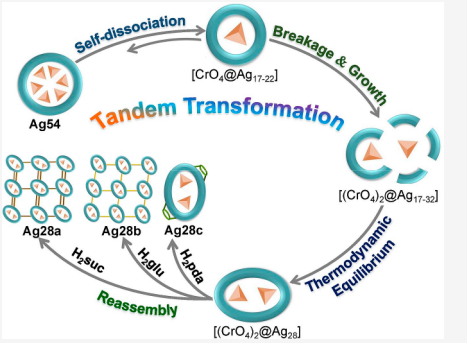

INTRODUCTION

The transformation chemistry of metal nanoclusters (NCs) at the atomic level represents the most ambitious dream in the cluster field.[1−4] The accessibility of precise formulas, high molecular purity, and the continuous advances in mass spectrometry, X-ray absorption fine structure (XAFS) analysis, small-angle X-ray scattering (SAXS) analysis,[5−8] single-crystal X-ray diffraction (SCXRD) analysis, and theoretical studies open up opportunities for researchers to investigate the transformation chemistry and establish structure−reactivity relationships of metal NCs at the atomic level.[9−14] Ligand-exchange-induced structure transformation (LEIST) has been proven to be an effective approach for manipulating the structure, size, and composition of NCs.[15,16] The LEIST generally entails the partial or complete substitution of the surface ligands with foreign ligands while retaining the original size of the NC core.[17−20] In some cases, the ligand exchange may also cause shape or size transformation of the NC core. For instance, Jin et al. performed the ligand exchange on $[Au_{38}(SCH_2CH_2Ph)_{24}]$ with HSPh-Bu^t and obtained another stable $[Au_{36}(SPh\text{-}Bu^t)_{24}]$.[21] Likewise, the Bakr group reported the ligand exchange of $[Ag_{44}(SPhF)_{30}]^{4-}$ (SPhF: 4-fluorobenzenethiolate) with 2,4-dimethylbenzenethiol ($HSPhMe_2$), forming a smaller $[Ag_{25}(SPhMe_2)_{18}]^-$.[22] The changes in structure and/or size of these metal NCs are most likely to be achieved by the thermally activated disproportionation of unstable intermediates in the presence of excessive foreign ligands.[21] What happens when a metal NC encounters a foreign ligand? Is it just a ligand exchange, or does the transformation of the cluster core change as well? If the latter is the case, then what is the transformation route from one to another? All of these are matters of deep investigation.

In addition, the prerequisite for understanding the precise transformation of metal NCs is to design and develop atomically accurate precursors built from a flexible ligand shell.[15,16] According to the classical "hard and soft acids and bases" (HSAB) principle, the carboxylate ligands are hard bases as compared to soft thiolate or alkyl moieties.[23] As a consequence, the coordination of the carboxylates with silver atoms is relatively weak; thus, they can be partially or completely exchanged with newly added ligands. More

Received: January 31, 2023
Published: August 30, 2023

recently, the PhCOOH-induced transformation was illustrated by our group, leading to the enlargement of both the inner anion template ($Mo_6O_{22}^{8-} \rightarrow Mo_8O_{28}^{8-}$) and the outer silver shell ($Ag_{44} \rightarrow Ag_{50}$).[24] We also demonstrated carboxylic acid-induced silver shell isomerism in a unique core−shell Ag_{84} NC.[25] All of these findings suggest that carboxylate ligands can induce the structural transformation of silver NCs, possibly initializing from ligand exchange under appropriate reaction conditions. Although the initial and final products of structural transformation have been isolated in the thiolate-protected gold/silver NCs,[26−32] the intermediates have rarely been studied, especially in alkynyl-stabilized silver NCs. A great difficulty in comprehending transformation processes arises from the fact that many transient intermediates are hard to isolate and thus cannot be characterized experimentally. Fortunately, time-dependent ESI-MS can give useful information about the evolution of species by in situ tracking of the transformation reaction process involving the changes in their composition and charge state, which allows us to deduce the complex transformation mechanisms. As stimulants, we used flexible dicarboxylates, which can replace the original monocarboxylate and then connect the adjacent silver NCs to unusual self-assembled structures.[33−36] Furthermore, an in-depth understanding of transformations, such as how to initiate the transformation by dicarboxylates, where the reaction sites are, how the transformation is completed from one intermediate to another, and how it ends up as the final thermodynamically stable product, is worth exploring.

Encouraged by our previous experiences[24,25,37−39] and the above considerations, in this work, we synthesized soft/hard mixed-ligand shell-protected **Ag54** and demonstrated its unexpected structural transformations with exogenous dicarboxylates such as H_2suc (succinic acid), H_2glu (glutaric acid), and H_2pda (2,2′-(1,2-phenylene)diacetic acid). More interestingly, **Ag54** first undergoes self-dissociation, and then the addition of H_2suc or H_2glu promotes the structural transformations to form 2D networks, **Ag28a** and **Ag28b**, respectively. However, the bulkier aromatic dicarboxylic acid H_2pda leads to the discrete silver nanocluster, **Ag28c**. ESI-MS and UV−vis studies have been used to understand the transformation pathways and establish the final "tandem transformation" (TT) mechanism. All the structures before and after transformations as well as one of the key intermediates were confirmed by SCXRD, and some other key intermediates were deduced by ESI-MS.

RESULTS AND DISCUSSION

The presence of labile carboxylates on the ligand shell of silver NC enables them to be used as flexible precursors to investigate transformation chemistry or reactivity at the atomic level under exotic stimuli. Extensive availability and a diverse range of carboxylic acids provide more opportunities to screen the reactivity of silver NCs. Typically, carboxylate-protected silver NCs have low nuclearity and are unstable.[40,41] To overcome these issues, we have used alkynyl as a coligand to improve the nuclearity, skeleton rigidity, and overall stability of the metal NCs.[42] The cluster precursor **Ag54** was synthesized by the reaction of polymeric $[^tBuC{\equiv}CAg]_n$, Ag_2O, ^{n}PrCOOH, and $K_2Cr_2O_7$ under solvothermal conditions in MeCN/ACE (acetonitrile/acetone). After the reaction, red block crystals were isolated with a yield of 35%. Although **Ag54** is a thermodynamically stable species after self-assembly, the labile carboxylate ligands on the surface can be replaced by ligands of stronger coordination and linkage ability under exotic stimuli, thereby forming new thermodynamically stable products, which may provide a new design blueprint for the synthesis of silver NCs. Inspired by this, we chose dicarboxylic acids as stimuli in the transformation reaction, mainly because of their substitution effect and bridging role as a dipodal linker, which can connect adjacent silver NCs to form cluster-based networks.[33−36] We speculate that there would be a dynamic competition reaction between mono- and dicarboxylic acids in the early stages of structural transformation and self-assembly. Some metastable species are first formed by competitive coordination self-assembly and can be further transformed to thermodynamically more stable products. Therefore, we treated the crystals of **Ag54** under the solvothermal condition with different dicarboxylic acids, such as H_2suc, H_2glu, and H_2pda, to construct **Ag28a**, **Ag28b**, and **Ag28c**, respectively (Scheme 1). All of the compounds were characterized by

Scheme 1. Top: Synthesis Route for Ag54 and the Following Transformation to Ag28a−Ag28c; Bottom: Photographs of Crystals Taken under the Microscope[a]

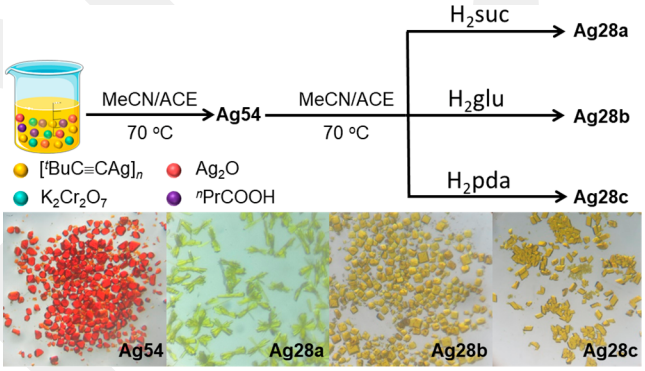

[a]MeCN = acetonitrile; ACE = acetone; H_2suc = succinic acid; H_2glu = glutaric acid; H_2pda = 2,2′-(1,2-phenylene)diacetic acid.

infrared (IR), energy dispersive X-ray (EDX) with elemental mapping, SCXRD, ESI-MS, UV−vis, and electrochemical analyses. The IR vibrations at 844 cm^{-1}, **Ag54**; 832 cm^{-1}, **Ag28a**; 832 cm^{-1}, **Ag28b**; and 834 cm^{-1}, **Ag28c** confirmed the presence of the CrO_4^{2-} ion, and the bands at 2021 cm^{-1}, **Ag54**; 2015 cm^{-1}, **Ag28a**; 2019 cm^{-1}, **Ag28b**; and 2012 cm^{-1}, **Ag28c** were assigned to the $^tBuC{\equiv}C^-$ moiety (Figure S1).[43,44]

X-ray Structures of Ag54 and Ag28a−Ag28c. SCXRD analysis reveals that the metallic skeleton of **Ag54** is a drumlike C_3 symmetric core−shell structure with a composition of $[K@(CrO_4)_6@Ag_{54}]$, which is protected by 18 ^{n}PrCOO$^-$ and 24 $^tBuC{\equiv}C^-$ ligands (Figure 1a). **Ag54** crystallizes in trigonal space group $R\bar{3}$ with a 3-fold rotoinversion axis passing through two polar H_2O molecules and a central K^+ ion, yielding only one-sixth of the cluster in an asymmetric unit. As shown in Figure 1b, K^+ is coordinated with 12 O atoms (K−O: 2.91−2.95 Å) from six CrO_4^{2-} ions, creating a $[K@(CrO_4)_6]$ core. The most significant difference between $[K@(CrO_4)_6@Ag_{54}]$ and the similar $[(MoO_4)_6@Ag_{55}]$ is that one central Ag^+ is wrapped by six MoO_4^{2-} through Ag−O bonds (2.70 Å).[45] Note that K^+ in **Ag54** should be from $K_2Cr_2O_7$, and the presence of K^+ was further confirmed by ESI-MS and elemental mapping (Figure S2) as discussed later. Excluding the K^+ ion, the distance between two O atoms on opposite

https://doi.org/10.1021/jacs.3c01119
J. Am. Chem. Soc. 2023, 145, 19523−19532

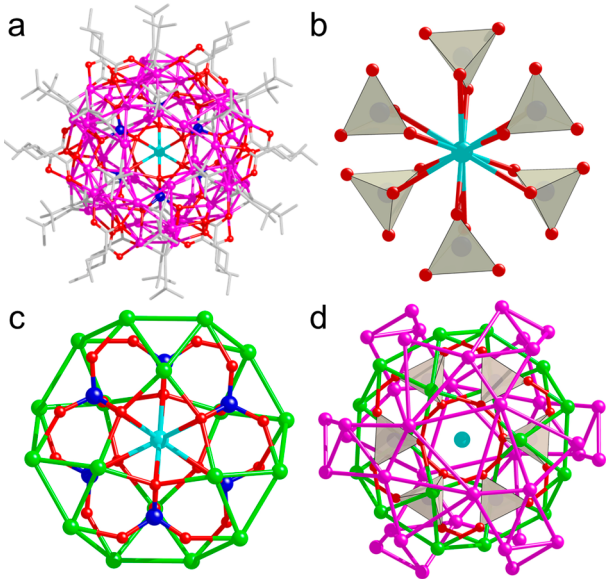

Figure 1. (a) Total crystal structure of **Ag54**. (b) $[K@(CrO_4)_6]$ core in **Ag54**. (c) $[K@(CrO_4)_6@Ag_{18}]$ subshell in **Ag54**. (d) $[K@(CrO_4)_6@Ag_{18}@Ag_{36}]$ multishell in **Ag54**. Hydrogen atoms are omitted for clarity. Color code: Ag, purple and green; K, cyan; Cr, blue; C, light gray; O, red; and CrO_4^{2-} tetrahedron, light yellow.

sides of the cavity is ~5.9 Å, and the cavity height is ~9.5 Å (Figure S3a). The cavity size is much larger than the ionic diameter of the alkali and alkaline earth metals ($Cs^+ > Rb^+ > K^+ > Ba^{2+} > Sr^{2+} > Na^+ > Ca^{2+} > Li^+ > Mg^{2+}$). Given the large cavity size, we then carried out the reactions under identical conditions in the presence of Cs^+ (d = 3.34 Å) and Ca^{2+} (d = 2.00 Å) ions to obtain Ag_{54} clusters (**Ag54-Cs** and **Ag54-Ca**). Importantly, the crystal structures of **Ag54-Cs** and **Ag54-Ca** are similar to that of **Ag54**, which suggests that the cavity is flexible and can trap other metal ions (Figure S3b and c).

The negatively charged $[K@(CrO_4)_6]$ core further pulls 18 Ag^+ ions around it via electrostatic interaction by forming Ag−O bonds (Ag−O: 2.15−2.61 Å) to build a positively charged subshell of $[K@(CrO_4)_6@Ag_{18}]$ (Figure 1c), which is enwrapped by an outer Ag_{36} cage to form the final multishell cluster $[K@(CrO_4)_6@Ag_{18}@Ag_{36}]$ (Figure 1d). The Ag···Ag interactions (2.87−3.30 Å) and Ag−O bonds (2.22−2.74 Å) additionally reinforce the stability of silver shells.[46−49] **Ag54** is further stabilized by 24 ^{t}BuC≡C$^-$ ligands, which exhibit μ_3-η_σ^1:η_σ^1:η_σ^1, μ_4-η_σ^1:η_σ^1:η_σ^1:η_σ^1, and μ_4-η_π^1:η_π^1:η_σ^1:η_σ^1 ligation modes with Ag−C distances of 2.11−2.49 Å.[50] Among them, 12 μ_3 ^{t}BuC≡C$^-$ ligands build 12 silver trigons on the surface of the Ag_{36} shell, and the other 12 μ_4 ^{t}BuC≡C$^-$ ligands connect the middle Ag_{18} and the outer Ag_{36} shell (Figure S4). To sum up, CrO_4^{2-} acts as a binder and stabilizer to connect the inner K^+, the middle Ag_{18} shell, and the outer Ag_{36} shell via Ag−O bonds. Interestingly, all the ^{n}PrCOO$^-$ ligands not only are on the surface of the outer Ag_{36} shell but also act as a glue that connects the Ag_{18} and Ag_{36} shells through Ag−O bonds with the coordination modes of six μ_3-κ^2:κ^1 and 12 μ_4-κ^3:κ^1 (Figure S5).

Based on the above structure analysis, we speculate that the ^{n}PrCOO$^-$ on the surface of **Ag54** may be easy to dissociate in solution, which motivated us to employ the different dicarboxylic acids as stimuli to screen its reactivity, which produced a new silver NC (**Ag28c**) and two cluster-based networks (**Ag28a** and **Ag28b**). Fortunately, we obtained high-quality crystals of three products after the transformation reactions. Structural studies show that **Ag28a** and **Ag28c** crystallize in triclinic space group $P\bar{1}$, whereas **Ag28b** crystallizes in orthorhombic space group *Pccn*. All of them are the analogous peanut-shaped Ag_{28} clusters, interiorly templated by a pair of CrO_4^{2-} ions (Figure 2a) and exteriorly

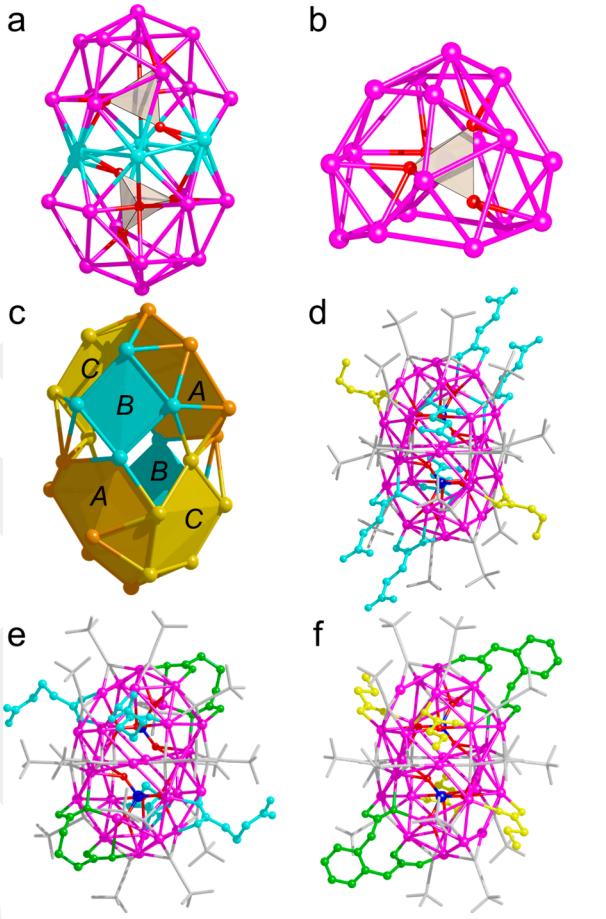

Figure 2. (a) Ball-and-stick view of $[(CrO_4)_2@Ag_{28}]$ with CrO_4^{2-} highlighted by the light yellow tetrahedron. (b) Ball-and-stick view of the $[(CrO_4)@Ag_{17}]$ unit with CrO_4^{2-} highlighted by the light yellow tetrahedron. (c) Schematic illustration of the coordination regions (***A***, ***B***, and ***C***) of carboxyl groups. The structure of the Ag_{28} cluster in (d) **Ag28a** and (e) **Ag28b**. (f) Total crystal structure of **Ag28c**. The bridging suc^{2-} and glu^{2-} are shown in cyan. The nonbridging glu^{2-} and pda^{2-} ligands are shown in green. The terminal ^{n}PrCOO$^-$ ligands are shown in yellow. Hydrogen atoms are omitted for clarity. Color code: Ag, purple, yellow, orange, and cyan; Cr, blue; O, red; C, light gray.

protected by ^{t}BuC≡C$^-$ and different carboxylates. Structures of all the Ag_{28} clusters could be seen as two fused $[(CrO_4)@Ag_{17}]$ units (Figure 2b) by sharing a chairlike hexagon (cyan Ag atoms, Figure 2a). In these structures, there are 16 ^{t}BuC≡C$^-$ ligands showing similar coordination modes (Figure S6). For instance, in the case of **Ag28c**, six ^{t}BuC≡C$^-$ ligands with four in μ_4-η_π^1:η_σ^1:η_σ^1:η_σ^1 and two in μ_3-η_σ^1:η_σ^1:η_σ^1 coordination mode are connected with silver atoms at the waist, and the other 10 ^{t}BuC≡C$^-$ ligands are coordinated with silver trigons in the pole and waist region of Ag_{28} through coordination modes of μ_3-η_π^1:η_σ^1:η_σ^1 and μ_3-η_σ^1:η_σ^1:η_σ^1 (Figure S6c and d).

The difference between them lies in the type, amount, and arrangement of carboxylates on the surface of the Ag_{28} cluster.

https://doi.org/10.1021/jacs.3c01119
J. Am. Chem. Soc. 2023, 145, 19523−19532

Notably, all carboxylates are site-specific and selectively bind to specific regions (*A*, *B*, and *C*) in **Ag28a**–**Ag28c**. Two carboxyl groups are capped on the silver heptagon *A* along with a ^{t}BuC≡C^{-} ligand, while one carboxyl group is capped on the silver tetragon *B* or silver pentagon *C* (Figure 2c and Figure S7). For **Ag28a**, the ^{n}PrCOO^{-} ligands are capped on the silver pentagon *C* by the μ_3-κ^1:κ^2 ligation mode. All of the suc^{2-} ligands adopt a μ_3-κ^1:κ^2 mode to cap on silver heptagon *A* or silver tetragon *B* and further bridge the adjacent clusters (Figure 2d and Figure S7). The torsion angles of C24–C39–C32–C19 and C3–C2–C2^{i}–C3^{i} of suc^{2-} are 177.98° and −180.00°, indicating an *anti* conformation from the perspective of stereochemistry.[33,34,51] The Ag–O$_{carboxylate}$ bond distances lie in the range of 2.15–2.54 Å. Finally, each Ag_{28} cluster is connected to four neighbors by six suc^{2-} ligands, forming a 2D 4^4-***sql*** lattice (Figure 3a).

The interesting feature of **Ag28b** is that the original ^{n}PrCOO^{-} has been completely substituted by glu^{2-}. Of note, two symmetry-related glu^{2-} ligands adopt a *gauche*–*gauche* conformation (torsion angles: C43–C44–C45–C46, −60.74°; C44–C45–C46–C47, 84.36°) and fold to staples (green colored) anchoring on the silver heptagon *A* of the Ag_{28} cluster via a μ_5-κ^1:κ^2:κ^1:κ^2 coordination mode.[33,34,52] In contrast, the other four glu^{2-} ligands (cyan) also adopt a *gauche*–*gauche* conformation (torsion angles: C54–C55–C56–C57, −71.64°; C55–C56–C57–C58, −68.19°), but they act as linear linkers (μ_3-κ^1:κ^2, Figure 2e) to connect four adjacent Ag_{28} clusters at silver tetragon *B* and pentagon *C* to form a 2D 4^4-***sql*** lattice (Figure 3b).

More interestingly, the regions occupied by four bridging glu^{2-} ligands in **Ag28b** are covered by four terminal ^{n}PrCOO^{-} ligands in **Ag28c** now. Two pda^{2-} ligands act as staples to lie on the surface of the Ag_{28} cluster through a μ_5-κ^1:κ^1:κ^1:κ^2 ligation mode[53] (green colored, Figure 2f). The staplelike pda^{2-} ligands prevent the further connection between adjacent clusters and eventually build a discrete cluster. By comparing the structures of **Ag28a**–**Ag28c**, we conclude that the conformation and carbon chain length of the dicarboxylates significantly impact the self-assembly between clusters.

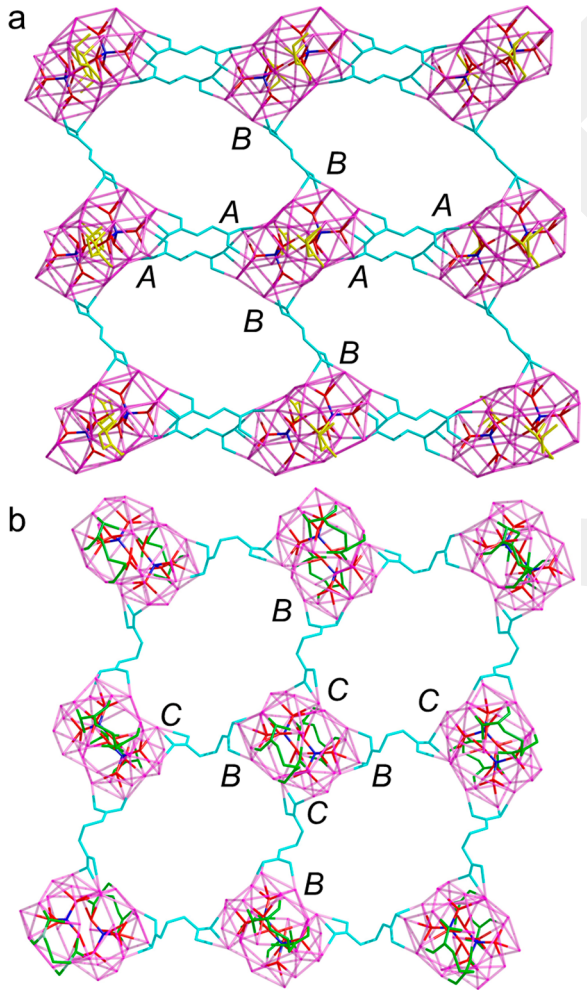

Figure 3. 2D 4^4-***sql*** lattice containing [(CrO$_4$)$_2$@Ag$_{28}$] clusters of (a) **Ag28a** and (b) **Ag28b**. The bridging suc^{2-} ligands are shown in cyan. The ^{n}PrCOO^{-} ligands are shown in yellow. The bridging and nonbridging glu^{2-} ligands are shown in cyan and green, respectively. Color code: Ag, purple; Cr, blue; and O, red. The *A*, *B*, and *C* represent the bridging sites of suc^{2-} or glu^{2-} ligands.

ESI-MS of Ag54 and Ag28a–Ag28c. To shed light on the solution behaviors, ESI-MS of **Ag54** was conducted in positive ion mode. The ESI-MS of a freshly prepared dichloromethane (DCM) solution of **Ag54** features the most prominent peak **1a** centered at 10074.8423, which is assigned to [K@(CrO$_4$)$_6$@Ag$_{54}$(^{t}BuC≡C)$_{24}$(^{n}PrCOO)$_{18}$]$^{+}$ (calcd 10074.8532), corresponding to the parent composition of **Ag54** (Figure 4a). Besides, six envelopes (**1b**–**1g**) totaling 14 singly charged species with very low abundance in the range of m/z = 3000–4200 were also observed. When the envelope is expanded, its shape except for **1b** deviates from the Gauss distribution, indicating the overlap of more than one species in it, which makes ESI-MS analysis more challenging. Each envelope can be divided into two or three species after careful analysis of the experimental mass spectra with calculated isotope distributions. The detailed assignment of each labeled species (**1b**–**1g**) is verified by isotope analysis, which perfectly matches the theoretical isotope distributions (Figure S8).

For **1b**, the signal centered at m/z = 3104.2012 corresponds to [(CrO$_4$)@Ag$_{17}$(^{t}BuC≡C)$_{11}$(^{n}PrCOO)$_3$]$^{+}$ (calcd 3104.2143). The adjacent envelope **1c** comprises **1c^1** and **1c^2**, which can be assigned to [(CrO$_4$)@Ag$_{18}$(^{t}BuC≡C)$_{12}$(^{n}PrCOO)$_3$]$^{+}$ (expt 3292.1666, calcd 3292.1899) and [(CrO$_4$)@Ag$_{18}$(^{t}BuC≡C)$_{11}$(^{n}PrCOO)$_4$]$^{+}$ (expt 3298.1410, calcd 3298.1640), respectively, which indicate one ^{t}BuC≡CAg (187.97) and ^{n}PrCOOAg (193.94) are appended to **1b**, forming **1c^1** and **1c^2**, respectively (Figure S8). The mass difference of 6 between **1c^1** and **1c^2** reveals the ligand exchange between one ^{n}PrCOO^{-} (87.04) and one ^{t}BuC≡C^{-} (81.06). Similarly, small fragment exchanges such as ^{t}BuC≡C^{-} and ^{n}PrCOO^{-} also occur between the species in **1e**, **1f**, and **1g** envelopes. Based on the analysis of **1b**–**1g**, we found that the Ag_{54} cluster showed a small fraction of self-dissociation equilibrated with the dominant composition of **1a** in solution; still, most fragments are silver clusters templated by a single CrO_4^{2-} ion. To gain deep insight into the stability of **Ag54** in solution, time-dependent ESI-MS was recorded under the same instrument parameters. Of note, the abundance of signals **1b**–**1g** increases, whereas **1a** decreases with the evolution of time (Figure 4b) without adding H_2suc, which indicates that **Ag54** is prone to self-dissociate in solution over time due to the labile nature of its ^{n}PrCOO^{-} ligand. Based on this observation, we can also rule out the fragmentation caused by the ESI process.

https://doi.org/10.1021/jacs.3c01119
J. Am. Chem. Soc. 2023, 145, 19523–19532

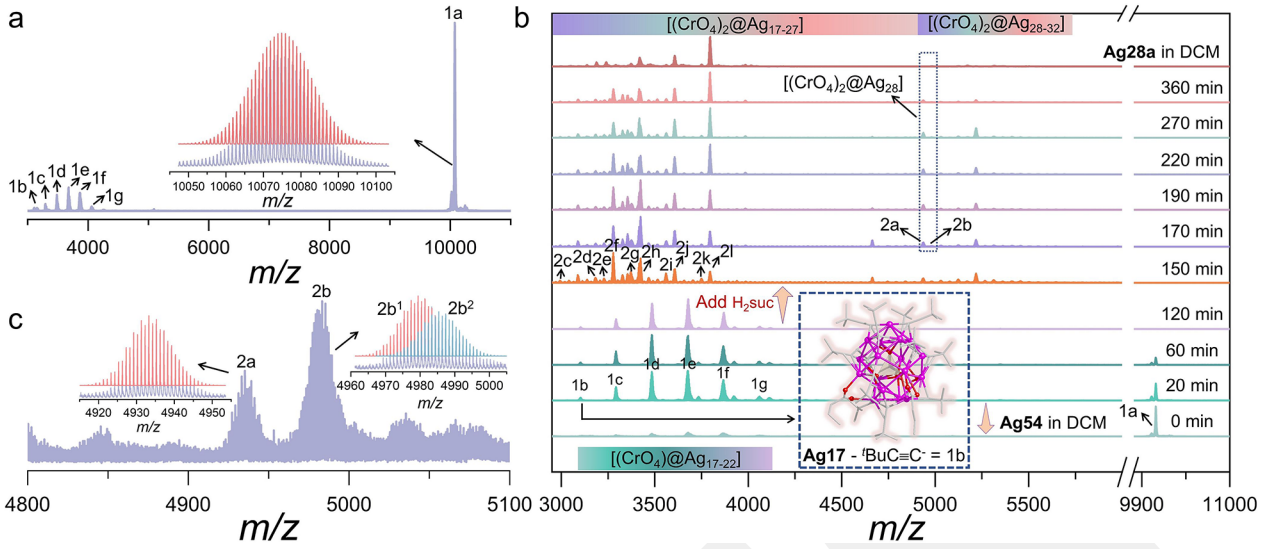

Figure 4. Positive ion mode ESI-MS of (a) **Ag54** dissolved in DCM. Inset: the experimental (light purple) and simulated (red/blue) isotopic distribution patterns for species **1a**. (b) Time-dependent ESI-MS of self-dissociation of **Ag54** before adding H_2suc (0−120 min) and the transformation from **Ag54** to **Ag28a** induced by adding H_2suc (120−360 min). (c) Enlarged ESI-MS of **Ag28a** dissolved in DCM. Insets: the experimental (light purple) and simulated (red/blue) isotopic distribution patterns for species **2a**, and **2b** (**2b**^{1} and **2b**^{2}).

Understanding the transformation mechanism triggered by the exotic ligands is crucial in exploring the synthesis, reactivity, and stability of metal NCs.[54−56] Recently, ESI-MS has become the most extensive and reliable technique for studying transformation mechanisms by tracking the reaction intermediates.[57,58] As mentioned above, **Ag54** initially exhibits a self-dissociation process due to the labile binding of ^{n}PrCOO$^-$. We envisioned that the foreign competitive ligands could interrupt the original coordination−dissociation equilibrium, yielding new products from **Ag54** during the postsynthetic transformation process. Therefore, we monitored the evolution of solution species upon adding the representative H_2suc to the DCM solution of **Ag54** through time-dependent ESI-MS. To ensure comparability of the intensity signals of each species at different time intervals, generalized operations for the sampling and analysis are realized and unified instrumentations are retained.

At different time intervals, 200 μL of the reaction mixture was extracted, diluted with 500 μL of DCM, and then quickly injected into the mass spectrometer for analyses. The ESI-MS of crystalline **Ag54** (light blue line) and **Ag28a** (red line) in DCM are also included in Figure 4b to fix the baseline and finishing line for this monitoring process. Based on experimental and theoretical isotopic distributions, the formulas of all labeled species are confirmed through isotope analysis and are listed in Figures S9 and S10.

It is worth noting that after 30 min of adding H_2suc (150 min, orange line in Figure 4b) to the self-dissociated solution of **Ag54**, the abundance of the signals corresponding to **1b−1g** gradually decreases with the progress of the reaction and finally disappears, while new signals (**2c−2l**) assigned to $[(CrO_4)_2@Ag_{17-21}]$ appear in the range m/z = 2950−4900 (Figure S9). Besides, larger species Ag_{28} (**2a** and **2b**) and Ag_{29}−Ag_{32} (**2m−2z**, Figure S10) were also detected. Two ^{t}BuC≡C$^-$ to one suc^{2-} ligand exchanges occurred between these adjacent species. Expanding the m/z range of 4910−5000 gave two peaks with a small fraction overlap, which are assigned to $[(CrO_4)_2@Ag_{28}(^t\text{BuC}{\equiv}\text{C})_{15}(\text{suc})_4]^+$ (**2a**), $[(CrO_4)_2@Ag_{28}(^t\text{BuC}{\equiv}\text{C})_{17}(\text{suc})_3]^+$ (**2b**^{1}), and $[(CrO_4)_2@Ag_{28}(^t\text{BuC}{\equiv}\text{C})_{16}(\text{suc})_3(^n\text{PrCOO})]^+$ (**2b**^{2}). Similar isotope patterns are also observed in the ESI-MS of **Ag28a** dissolved in DCM (Figure 4c). Among them, **2b**^{2} can be regarded as the building unit of **Ag28a** after losing one ^{n}PrCOO$^-$. The expanded view of peaks (**2m−2z**) corresponding to the $[(CrO_4)_2@Ag_{29-32}]$ species in the m/z range 5000−5700 is shown in Figure S10. The acid-induced transformation process from $[(CrO_4)@Ag_{17-22}]$ to $[(CrO_4)_2@Ag_{17-32}]$ involves ligand shell variation, metal skeleton rearrangement, and the inclusion of a single template into double templates. During the self-assembly of complex architectures, it is clear that many dynamically competitive metastable intermediates may form before the final thermodynamically stable product forms.

Furthermore, as the reaction proceeds (170−360 min), the abundance of small species, including $[(CrO_4)_2@Ag_{17-20}]$ (**2c−2k**), gradually decreases, while that of $[(CrO_4)_2@Ag_{21}]$ (**2l**) becomes stronger. The mass spectrum of the reaction mixture (360 min) is quite similar to that of **Ag28a**, suggesting the complete transformation from **Ag54** to **Ag28a**. It is concluded that $[(CrO_4)@Ag_{17-22}]$ (**1b−1g**) species are prone to transformation into $[(CrO_4)_2@Ag_{17-32}]$ (**2a−2z**) species when stimulated with H_2suc, of which $[(CrO_4)_2@Ag_{28}]$ was finally selected as a thermodynamically stable product to be trapped by a new ligand shell and then extended to the 2D network. To better understand the structure transformation from Ag_{54} to Ag_{28}, we attempted to recrystallize **Ag54** in a binary solvent of DCM and MeCN, similar to the solvent system under the ESI-MS conditions. Fortunately, yellow block crystals (**Ag17**) were isolated at −18 °C, and the corresponding molecular structure identification by SCXRD reveals that it crystallizes in the triclinic system with space group $P\bar{1}$ and can be formulated as $(CrO_4)@Ag_{17}(^t\text{BuC}{\equiv}\text{C})_{12}(^n\text{PrCOO})_3$, which is similar to half of the peanut-shaped Ag_{28} cluster (Figure S11). Furthermore, after removal of a ^{t}BuC≡C$^-$ ligand, the composition of **Ag17** is exactly equal to that of **1b** that was detected in the self-dissociation process of **Ag54** by ESI-MS, representing a key intermediate in the structural transformation from Ag_{54} to Ag_{28}.

https://doi.org/10.1021/jacs.3c01119
J. Am. Chem. Soc. 2023, 145, 19523−19532

Based on the above results, the transformation process can be described as a TT mechanism and can be roughly divided into four steps: (i) The Ag_{54} silver shell is broken into $[(CrO_4)@Ag_{17-22}]$ species by self-dissociation; (ii) H_2suc induces the breakage and growth of the above-mentioned $[(CrO_4)@Ag_{17-22}]$ to $[(CrO_4)_2@Ag_{17-32}]$ species; (iii) $[(CrO_4)_2@Ag_{28}]$ is thermodynamically selected as the main product with the help of a new ligand combination; (iv) each $[(CrO_4)_2@Ag_{28}]$ is connected with four adjacent Ag_{28} clusters through six sharing suc^{2-} to generate a 2D network (Figure 5).

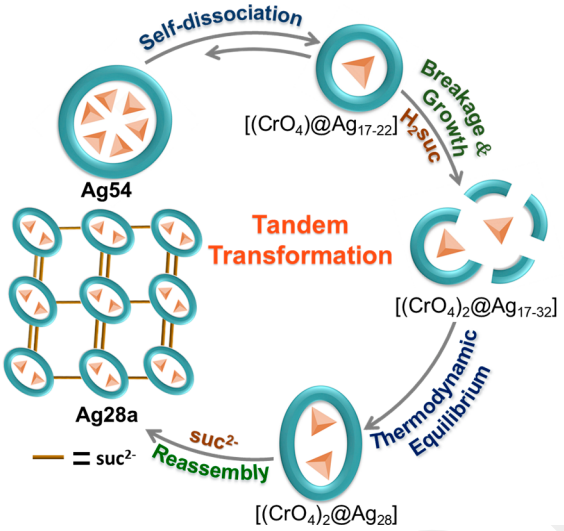

Figure 5. Proposed mechanism for the transformation from **Ag54** to **Ag28a**. The orange tetrahedron, blue shell, and brown rod represent CrO_4^{2-}, silver shell, and suc^{2-}, respectively.

Optical Properties of Ag54 and Ag28a−Ag28c. The optical properties of cluster precursors and their ensuing products of identical cores with different protecting ligands could be of interest for potential applications. The optical absorption spectra of all of the compounds were recorded in the solid state. As shown in Figure S12, all the compounds exhibit a broad absorption band near 420 and 350 nm, which may be assigned to the ligand-to-metal charge transfer (LMCT) and $\pi-\pi^*$ transitions of the ^{t}BuC≡C$^-$ ligands, respectively.[59] Furthermore, the optical band gaps of **Ag54** and **Ag28a−Ag28c** were determined to be 1.94, 2.19, 2.16, and 2.13 eV, respectively, by using the transformed Kubelka−Munk function and Tauc plot.

The mechanism of how the dicarboxylate initiates the transformation process has been further supported by UV−vis absorption spectroscopy (Figure 6). The DCM solution of **Ag54** (0 min) exhibits low- and high-energy bands at 420 and 229 nm, respectively, which may be assigned to the LMCT and $\pi-\pi^*$ transitions of the ^{t}BuC≡C$^-$ ligands, respectively. Between 20 and 120 min, a new shoulder band appears at 265 nm with a decreased absorbance at 420 nm, which clearly indicates the self-dissociation of **Ag54** and the emergence of new species. After the addition of H_2suc (0.1 mmol, 11.8 mg) to the self-dissociated solution of **Ag54**, the reaction progress is monitored as a function of time (120−360 min). At 150 min, the band at 265 nm disappeared with the broadening of the spectrum, and the color of the solution changed from orange-yellow to turbid and pale yellow (right in Figure 6). The complete transformation from Ag_{54} to Ag_{28} was achieved in

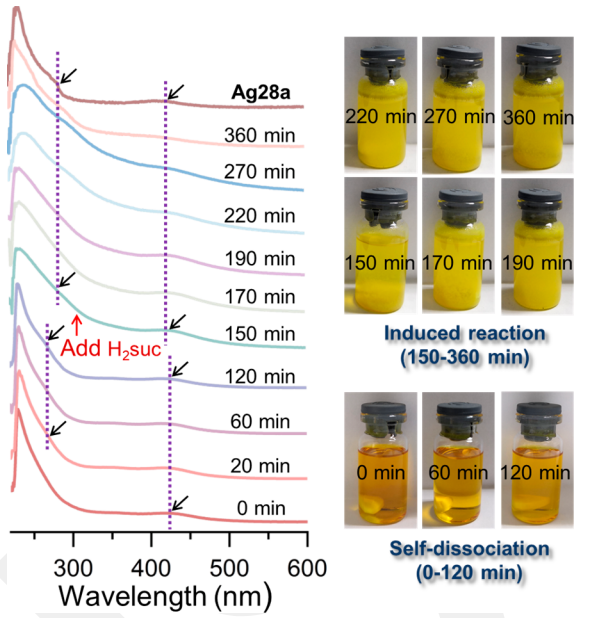

Figure 6. Time-dependent UV−vis absorption spectra for the transformation from **Ag54** to **Ag28a** induced by adding H_2suc. Photographs of the reaction mixture at different time points.

360 min of the reaction, with the appearance of a new band at 280 nm and a small blue shift of 420 nm to 416 nm. The corresponding spectrum (360 min) is similar to the original UV−vis spectrum of **Ag28a**.

Catalytic Reduction of 4-Nitrophenol (4-NP). Nitrophenols have stable physicochemical properties, high water solubility, strong migration ability, and a long half-life in the natural environment. They can be transmitted and enriched in aquatic organisms, accumulate, and remain in soil and water for a long time, causing great harm to the environment and human beings.[60,61] Therefore, the development of efficient, atomically precise catalysts for the reduction and decomposition of nitrophenols is highly required. The reduction of 4-NP to 4-aminophenol (4-AP) by $NaBH_4$ was used as a model reaction to assess the catalytic performance of **Ag54** and **Ag28a−Ag28c**. The reduction process was monitored by time-dependent UV−vis absorption spectra. After different catalysts were added into the mixture of 4-NP and $NaBH_4$, the absorption peak at 400 nm decreases as the reaction proceeds, indicating that all four of them are capable of reducing 4-NP to 4-AP (Figure 7a−d). Interestingly, **Ag28a−Ag28c** show significantly higher catalytic activity than **Ag54** (Figure 7e). For **Ag28b** and **Ag28c**, 4-NP can be completely reduced to 4-AP in ∼30 min, and for **Ag28a**, it took ∼55 min, whereas the reaction does not complete even after 3 h for **Ag54**. In these experiments, an excess amount of $NaBH_4$ was used compared to 4-NP, indicating that the reduction process is anticipated to follow a pseudo-first-order reaction, as depicted by the equation $\ln(C_t/C_0) = kt$ (Figure S13). In this equation, C_t and C_0 represent the concentrations of 4-NP at the reaction time and initial time, respectively, and k denotes the apparent rate constant. The k values, obtained from the plot of $\ln(C_t/C_0)$ versus time, were determined as 0.02, 0.07, 0.11, and 0.13 min^{-1} for **Ag54**, **Ag28a**, **Ag28b**, and **Ag28c**, respectively, following the sequence of **Ag28c** > **Ag28b** > **Ag28a** > **Ag54**.

To verify the first-order kinetics in this system and unveil the catalytic mechanism, we monitored the catalytic processes of

https://doi.org/10.1021/jacs.3c01119
J. Am. Chem. Soc. 2023, 145, 19523−19532

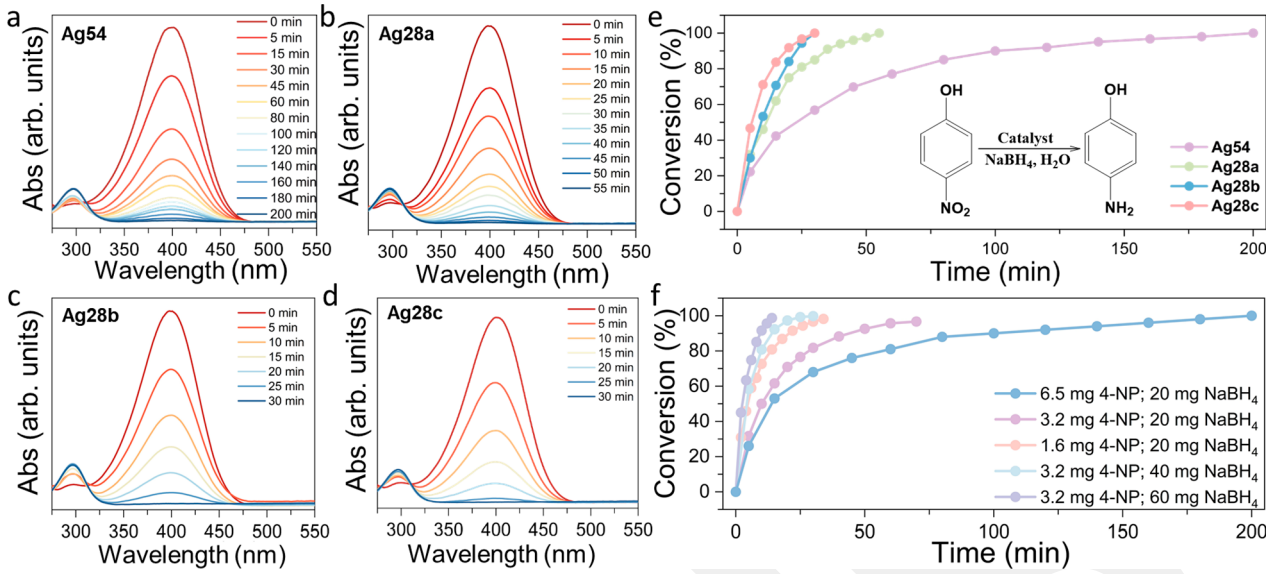

Figure 7. Catalytic properties of **Ag54** and **Ag28a**–**Ag28c**. Time-dependent UV–vis absorption spectra of 4-NP reduction by $NaBH_4$ in the presence of different catalysts: (a) **Ag54**, (b) **Ag28a**, (c) **Ag28b**, and (d) **Ag28c**. (e) The conversion versus time in the presence of **Ag54** and **Ag28a**–**Ag28c**. Conditions: 1 mg of catalysts, 6.5 mg of 4-NP, 20 mg of $NaBH_4$, and 3 mL of H_2O. (f) The conversion versus time in the presence of **Ag54** (1 mg) under different concentrations of 4-NP or $NaBH_4$.

Ag54 and **Ag28c** at different concentrations of 4-NP or $NaBH_4$ (Figure 7f and Figures S14–S18). Decreasing the amount of 4-NP or increasing the amount of $NaBH_4$ resulted in a corresponding increase in the reaction rate. This concentration-dependent catalytic behavior clearly demonstrates the competition between the two reactants for adsorption sites on the surface of the silver cluster. These findings exclude the concentration-independent Eley–Rideal mechanism and match well with the Langmuir–Hinshelwood (LH) mechanism.[62−64] Therefore, both reactants (BH_4^- and 4-NP) are simultaneously adsorbed on the cluster surface prior to the reaction. The adsorption of both reagents on the surface is fast and is modeled in terms of a Langmuir isotherm, as is widely accepted in the literature.[63,65] The adsorbed reactant species then undergo a reaction with each other, resulting in the formation of 4-AP, which subsequently detaches from the surface of the silver cluster. The rate-determining step in this process is the reduction of adsorbed 4-NP to 4-AP. The detachment of product 4-AP from the surface creates vacant sites, enabling the catalytic cycle to initiate again.

The high catalytic activities for **Ag28a**–**Ag28c** can be attributed to the greater number of exposed Ag atoms, which can provide greater accessibility for the adsorption and reaction sites for 4-NP and active hydrogen.[66] It is obvious that the number of exposed Ag atoms on the surface of **Ag28a**–**Ag28c** is higher than that of **Ag54** (Figures S19 and S20). The 2D networks of **Ag28a** and **Ag28b** may impede the absorption of 4-NP to some extent due to steric hindrance from the bridging dicarboxylates. Notably, the intercluster $C_{t\mathrm{BuC}\equiv\mathrm{C}}$–H···$O_{n\mathrm{PrCOOH}}$ (3.61 Å), C_{pda}–H···$O_{n\mathrm{PrCOOH}}$ (3.39 Å), and $O_{n\mathrm{PrCOOH}}$–H···O_{pda} (2.56 Å) hydrogen bonds generate a 1D supramolecular assembly that provides additional structural stability and absorption capacity to the **Ag28c** (Figure S21).

To gain a deeper understanding of the catalytic activity of clusters for the reduction of 4-NP, we perform density functional theory (DFT) calculations (see SI for calculation details) for the **Ag28c**-4-NP complex. As shown in Figure 8a, Ag atoms on the **Ag28c** cluster exhibit a strong positive electrostatic potential (ESP), as indicated by the ESP fitted CHELPG charges. In comparison, O atoms in 4-NP show negative ESP, providing an energetically favorable chemisorption process for the 4-NP molecule on the cluster, which is an essential step for the previously shown LH mechanism for the reduction of 4-NP.[67,68] The calculated adsorption energy (E_{ad}) is −0.24 eV, with nearest Ag–O distances of 2.91 and 3.01 Å. Furthermore, partial density of states (PDOS) curves (Figure 8b) and selective MOs (Figure 8c) indicate noticeable MO coupling in the **Ag28c**-4-NP complex, particularly between the Ag d (**Ag28c**) and the O p (4-NP) fragments. It is likely that this interaction is largely enhanced for **Ag28c** due to exposed Ag atoms compared with the case in **Ag54**, resulting in increased catalytic activity for **Ag28c**.

CONCLUSIONS

In summary, a flexible silver-alkynyl cluster synthon, **Ag54**, was created by the judicial selection of labile carboxylate coligands. This is the first report on the systematic investigation into how the dicarboxylates trigger transformation and where the reaction sites for silver clusters are available. More importantly, SCXRD was used to determine all of the structures before and after transformation, which revealed that **Ag54** was transformed into Ag_{28} cluster-based 2D networks induced by H_2suc and H_2glu, while with H_2pda, a discrete Ag_{28} cluster was isolated. Of note, the Ag_{54} cluster can be universally transformed into a similar peanut-shaped Ag_{28} by self-dissociation and reassembly, no matter what dicarboxylic acid is used. The mechanism of TT from **Ag54** to **Ag28a** has been established through time-dependent ESI-MS and UV–vis studies, along with the structural characterization of key intermediate **Ag17**, further validating the TT structural transformation mechanism. Furthermore, all of them have been used as catalysts for the catalytic reduction of 4-nitrophenol, and their catalytic activities have been improved through structural transformation. The present mechanism will not only allow rich opportunities for researchers to gain fundamental insights into the transformation chemistry of

https://doi.org/10.1021/jacs.3c01119
J. Am. Chem. Soc. 2023, 145, 19523−19532

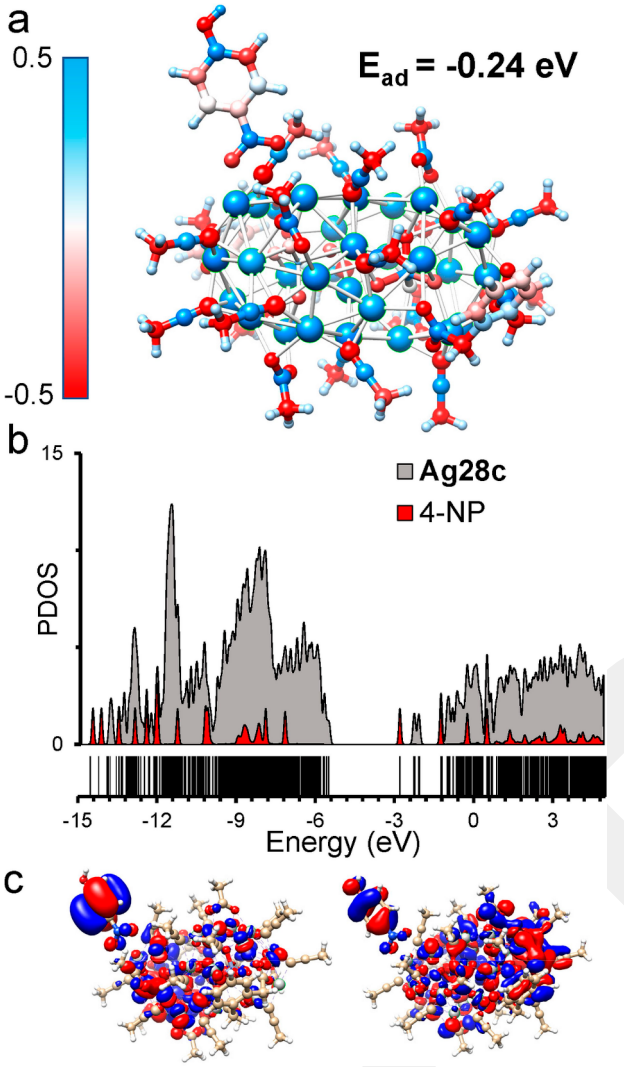

Figure 8. (a) Calculated CHELPG charges and adsorption energy for the optimized geometry of the **Ag28c**-NP complex. (b) PDOS curves for the **Ag28c**-NP complex, where HOMO and LUMO levels correspond to −5.49 and −2.79 eV, respectively, and (c) selected MOs indicating the Ag d and O p interaction for the **Ag28c**-NP complex.

clusters at the atomic level but also provide new ways to synthesize novel functional metal clusters and cluster-based polymeric materials with broader applications.

■ ASSOCIATED CONTENT

Supporting Information

The Supporting Information is available free of charge at https://pubs.acs.org/doi/10.1021/jacs.3c01119.

Experimental details, detailed crystallographic structure, and data including UV−vis, IR, and EDS mapping (PDF)

Accession Codes

CCDC 2129802, 2129805, 2129807, 2129809, 2239050−2239051, and 2256559 contain the supplementary crystallographic data for this paper. These data can be obtained free of charge via www.ccdc.cam.ac.uk/data_request/cif, or by emailing data_request@ccdc.cam.ac.uk, or by contacting The Cambridge Crystallographic Data Centre, 12 Union Road, Cambridge CB2 1EZ, UK; fax: +44 1223 336033.

■ AUTHOR INFORMATION

Corresponding Author

Di Sun − *School of Chemistry and Chemical Engineering, State Key Laboratory of Crystal Materials, Shandong University, Jinan 250100, People's Republic of China;* orcid.org/0000-0001-5966-1207; Email: dsun@sdu.edu.cn

Authors

Zhi Wang − *School of Chemistry and Chemical Engineering, State Key Laboratory of Crystal Materials, Shandong University, Jinan 250100, People's Republic of China;* orcid.org/0000-0001-8315-3501

Rakesh Kumar Gupta − *School of Chemistry and Chemical Engineering, State Key Laboratory of Crystal Materials, Shandong University, Jinan 250100, People's Republic of China;* orcid.org/0000-0002-5701-3449

Fahri Alkan − *Department of Nanotechnology Engineering, Abdullah Gül University, Kayseri 38080, Turkey;* orcid.org/0000-0002-4046-9044

Bao-Liang Han − *School of Chemistry and Chemical Engineering, State Key Laboratory of Crystal Materials, Shandong University, Jinan 250100, People's Republic of China;* orcid.org/0000-0002-4601-2600

Lei Feng − *School of Chemistry and Chemical Engineering, State Key Laboratory of Crystal Materials, Shandong University, Jinan 250100, People's Republic of China;* orcid.org/0000-0002-5309-1298

Xian-Qiang Huang − *Shandong Provincial Key Laboratory of Chemical Energy Storage and Novel Cell Technology, School of Chemistry and Chemical Engineering, Liaocheng University, Liaocheng 252059, People's Republic of China*

Zhi-Yong Gao − *School of Chemistry and Chemical Engineering, Henan Normal University, Xinxiang 453007, People's Republic of China;* orcid.org/0000-0002-2181-7402

Chen-Ho Tung − *School of Chemistry and Chemical Engineering, State Key Laboratory of Crystal Materials, Shandong University, Jinan 250100, People's Republic of China;* orcid.org/0000-0001-9999-9755

Complete contact information is available at: https://pubs.acs.org/10.1021/jacs.3c01119

Author Contributions

Z.W. and R.K.G. contributed equally.

Notes

The authors declare no competing financial interest.

■ ACKNOWLEDGMENTS

This work was financially supported by the National Natural Science Foundation of China (Grant Nos. 22201159, 22171164, 22325105, 52261135637), the Natural Science Foundation of Shandong Province (No. ZR2022QB008), the National Postdoctoral Innovative Talents Support Program (No. BX2021171), China Postdoctoral Science Foundation (No. 2021M700081), and the Instrument Improvement Funds of Shandong University Public Technology Platform (ts20220102). The DFT calculations reported in this paper were partially performed at TUBITAK ULAKBIM, High

Performance and Grid Computing Center (TRUBA resources).

REFERENCES

(1) Cook, A. W.; Hayton, T. W. Case Studies in Nanocluster Synthesis and Characterization: Challenges and Opportunities. *Acc. Chem. Res.* **2018**, *51*, 2456−2464.

(2) Jin, R.; Zeng, C.; Zhou, M.; Chen, Y. Atomically Precise Colloidal Metal Nanoclusters and Nanoparticles: Fundamentals and Opportunities. *Chem. Rev.* **2016**, *116*, 10346−10413.

(3) Nguyen, T.-A. D.; Jones, Z. R.; Leto, D. F.; Wu, G.; Scott, S. L.; Hayton, T. W. Ligand-Exchange-Induced Growth of an Atomically Precise Cu_{29} Nanocluster from a Smaller Cluster. *Chem. Mater.* **2016**, *28*, 8385−8390.

(4) Yan, L.-L.; Yao, L.-Y.; Yam, V. W.-W. Concentration- and Solvation-Induced Reversible Structural Transformation and Assembly of Polynuclear Gold(I) Sulfido Complexes. *J. Am. Chem. Soc.* **2020**, *142*, 11560−11568.

(5) Liu, X.; Yang, H.; Chen, Y.; Yang, Y.; Porcar, L.; Radulescu, A.; Guldin, S.; Jin, R.; Stellacci, F.; Luo, Z. Quantifying the Solution Structure of Metal Nanoclusters Using Small-Angle Neutron Scattering. *Angew. Chem., Int. Ed.* **2022**, *61*, No. e202209751.

(6) Kögerler, P.; Cronin, L. Polyoxometalate Nanostructures, Superclusters, and Colloids: From Functional Clusters to Chemical Aesthetics. *Angew. Chem., Int. Ed.* **2005**, *44*, 844−846.

(7) Malinenko, A.; Jonchère, A.; Girard, L.; Parrès-Maynadié, S.; Diat, O.; Bauduin, P. Are Keggin's POMs Charged Nanocolloids or Multicharged Anions? *Langmuir* **2018**, *34*, 2026−2038.

(8) Liu, T. Hydrophilic Macroionic Solutions: What Happens When Soluble Ions Reach the Size of Nanometer Scale? *Langmuir* **2010**, *26*, 9202−9213.

(9) Pei, Y.; Zeng, X. C. Investigating the Structural Evolution of Thiolate Protected Gold Clusters from First-Principles. *Nanoscale* **2012**, *4*, 4054−4072.

(10) Wang, J.; Wang, Z.-Y.; Li, S.-J.; Zang, S.-Q.; Mak, T. C. W. Carboranealkynyl-Protected Gold Nanoclusters: Size Conversion and UV/Vis-NIR Optical Properties. *Angew. Chem., Int. Ed.* **2021**, *60*, 5959−5964.

(11) Fernando, A.; Weerawardene, K. L. D. M.; Karimova, N. V.; Aikens, C. M. Quantum Mechanical Studies of Large Metal, Metal Oxide, and Metal Chalcogenide Nanoparticles and Clusters. *Chem. Rev.* **2015**, *115*, 6112−6216.

(12) Heinecke, C. L.; Ni, T. W.; Malola, S.; Mäkinen, V.; Wong, O. A.; Häkkinen, H.; Ackerson, C. J. Structural and Theoretical Basis for Ligand Exchange on Thiolate Monolayer Protected Gold Nanoclusters. *J. Am. Chem. Soc.* **2012**, *134*, 13316−13322.

(13) Malola, S.; Lehtovaara, L.; Häkkinen, H. A DFT Study of Linear Gold-Thiolate Superclusters Absorbing in the Therapeutic NIR Window. *J. Phys. Chem. Lett.* **2014**, *5*, 1329−1334.

(14) Zhang, P. X-ray Spectroscopy of Gold-Thiolate Nanoclusters. *J. Phys. Chem. C* **2014**, *118*, 25291−25299.

(15) Kang, X.; Zhu, M. Transformation of Atomically Precise Nanoclusters by Ligand-Exchange. *Chem. Mater.* **2019**, *31*, 9939−9969.

(16) Zeng, C.; Chen, Y.; Das, A.; Jin, R. Transformation Chemistry of Gold Nanoclusters: From one Stable Size to Another. *J. Phys. Chem. Lett.* **2015**, *6*, 2976−2986.

(17) AbdulHalim, L. G.; Kothalawala, N.; Sinatra, L.; Dass, A.; Bakr, O. M. Neat and Complete: Thiolate-Ligand Exchange on a Silver Molecular Nanoparticle. *J. Am. Chem. Soc.* **2014**, *136*, 15865−15868.

(18) McKenzie, L. C.; Zaikova, T. O.; Hutchison, J. E. Structurally Similar Triphenylphosphine-Stabilized Undecagolds, $Au_{11}(PPh_3)_7Cl_3$ and $[Au_{11}(PPh_3)_8Cl_2]Cl$, Exhibit Distinct Ligand Exchange Pathways with Glutathione. *J. Am. Chem. Soc.* **2014**, *136*, 13426−13435.

(19) Saruyama, M.; Sato, R.; Teranishi, T. Transformations of Ionic Nanocrystals via Full and Partial Ion Exchange Reactions. *Acc. Chem. Res.* **2021**, *54*, 765−775.

(20) Zhang, S.-S.; Liu, R.-C.; Zhang, X.-C.; Feng, L.; Xue, Q.-W.; Gao, Z.-Y.; Tung, C.-H.; Sun, D. Core Engineering of Paired Core-Shell Silver Nanoclusters. *Sci. China Chem.* **2021**, *64*, 2118−2124.

(21) Zeng, C.; Liu, C.; Pei, Y.; Jin, R. Thiol Ligand-Induced Transformation of $Au_{38}(SC_2H_4Ph)_{24}$ to $Au_{36}(SPh\text{-}t\text{-}Bu)_{24}$. *ACS Nano* **2013**, *7*, 6138−6145.

(22) Bootharaju, M. S.; Joshi, C. P.; Alhilaly, M. J.; Bakr, O. M. Switching a Nanocluster Core from Hollow to Nonhollow. *Chem. Mater.* **2016**, *28*, 3292−3297.

(23) Parr, R. G.; Pearson, R. G. Absolute Hardness: Companion Parameter to Absolute Electronegativity. *J. Am. Chem. Soc.* **1983**, *105*, 7512−7516.

(24) Wang, Z.; Su, H.-F.; Tung, C.-H.; Sun, D.; Zheng, L.-S. Deciphering Synergetic Core-Shell Transformation from $[Mo_6O_{22}@Ag_{44}]$ to $[Mo_8O_{28}@Ag_{50}]$. *Nat. Commun.* **2018**, *9*, 4407.

(25) Wang, Z.; Sun, H.-T.; Kurmoo, M.; Liu, Q.-Y.; Zhuang, G.-L.; Zhao, Q.-Q.; Wang, X.-P.; Tung, C.-H.; Sun, D. Carboxylic Acid Stimulated Silver Shell Isomerism in a Triple Core-Shell Ag_{84} Nanocluster. *Chem. Sci.* **2019**, *10*, 4862−4867.

(26) Hau, S. C. K.; Cheng, P.-S.; Mak, T. C. W. Enlargement of Globular Silver Alkynide Cluster via Core Transformation. *J. Am. Chem. Soc.* **2012**, *134*, 2922−2925.

(27) Kawawaki, T.; Ebina, A.; Hosokawa, Y.; Ozaki, S.; Suzuki, D.; Hossain, S.; Negishi, Y. Thiolate-Protected Metal Nanoclusters: Recent Development in Synthesis, Understanding of Reaction, and Application in Energy and Environmental Field. *Small* **2021**, *17*, 2005328.

(28) Li, Y.; Juarez-Mosqueda, R.; Song, Y.; Zhang, Y.; Chai, J.; Mpourmpakis, G.; Jin, R. Ligand Exchange on $Au_{38}(SR)_{24}$: Substituent Site Effects of Aromatic Thiols. *Nanoscale* **2020**, *12*, 9423−9429.

(29) Guan, Z.-J.; Hu, F.; Li, J.-J.; Wen, Z.-R.; Lin, Y.-M.; Wang, Q.-M. Isomerization in Alkynyl-Protected Gold Nanoclusters. *J. Am. Chem. Soc.* **2020**, *142*, 2995−3001.

(30) Yang, X.; Lin, X.; Liu, C.; Wu, R. a.; Yan, J.; Huang, J. Reversible Conversion between Phosphine Protected Au_6 and Au_8 Nanoclusters under Oxidative/Reductive Conditions. *Nanoscale* **2017**, *9*, 2424−2427.

(31) Yao, Q.; Fung, V.; Sun, C.; Huang, S.; Chen, T.; Jiang, D.-e.; Lee, J. Y.; Xie, J. Revealing Isoelectronic Size Conversion Dynamics of Metal Nanoclusters by a Noncrystallization Approach. *Nat. Commun.* **2018**, *9*, 1979.

(32) Zhang, B.; Chen, C.; Chuang, W.; Chen, S.; Yang, P. Size Transformation of the $Au_{22}(SG)_{18}$ Nanocluster and Its Surface-Sensitive Kinetics. *J. Am. Chem. Soc.* **2020**, *142*, 11514−11520.

(33) Choubey, S.; Roy, S.; Bhar, K.; Mitra, P.; Ribas, J.; Ghosh, B. K. Varied Dicarboxylate Bridges in Dinuclear Ttrigonal Prismatic Manganese(II) and Octahedral Nickel(II) Compounds Containing Tetradentate N-donor Schiff Bases: Syntheses, Structures and Magnetic Behaviors. *Polyhedron* **2014**, *74*, 134−143.

(34) Shyu, E.; Supkowski, R. M.; LaDuca, R. L. Structural Diversity in Luminescent Three-Dimensional Cadmium Aliphatic Dicarboxylate Coordination Polymers Incorporating 4,4′-Dipyridylamine: Interpenetrated, Non-Interpenetrated, and Self-Penetrated Networks. *Cryst. Growth Des.* **2009**, *9*, 2481−2491.

(35) Sun, D.; Li, Y.-H.; Hao, H.-J.; Liu, F.-J.; Zhao, Y.; Huang, R.-B.; Zheng, L.-S. Syntheses, Structures and Photoluminescent Properties of a Series of Ag(I) Coordination Architectures Based on 2,4-Diamino-6-Methyl-1,3,5-Triazine and Dicarboxylates: from a 0D Discrete Molecule to a 3D Infinite Network. *CrystEngComm* **2011**, *13*, 6431−6441.

(36) Wen, G.-L.; Wang, Y.-Y.; Zhang, W.-H.; Ren, C.; Liu, R.-T.; Shi, Q.-Z. Self-Assembled Coordination Polymers of V-Shaped Bis(pyridyl)Thiadiazole Dependent upon the Spacer Length and Flexibility of Aliphatic Dicarboxylate Ligands. *CrystEngComm* **2010**, *12*, 1238−1251.

(37) Li, X.-Y.; Su, H.-F.; Kurmoo, M.; Tung, C.-H.; Sun, D.; Zheng, L.-S. Structure, Solution Assembly, and Electroconductivity of

https://doi.org/10.1021/jacs.3c01119
J. Am. Chem. Soc. 2023, 145, 19523−19532

Nanosized Argento-Organic-Cluster/Framework Templated by Chromate. *Nanoscale* **2017**, *9*, 5305−5314.
(38) Sun, D.; Wang, D.-F.; Han, X.-G.; Zhang, N.; Huang, R.-B.; Zheng, L.-S. Stepwise Assembly of Two 3d-4d Heterometallic Coordination Polymers based on a Hexanuclear Silver(i) Metalloligand. *Chem. Commun.* **2011**, *47*, 746−748.
(39) Zhang, S.-S.; Alkan, F.; Su, H.-F.; Aikens, C. M.; Tung, C.-H.; Sun, D. $[Ag_{48}(C{\equiv}C^tBu)_{20}(CrO_4)_7]$: An Atomically Precise Silver Nanocluster Co-protected by Inorganic and Organic Ligands. *J. Am. Chem. Soc.* **2019**, *141*, 4460−4467.
(40) Liu, K.-G.; Gao, X.-M.; Liu, T.; Hu, M.-L.; Jiang, D.-E. All-Carboxylate-Protected Superatomic Silver Nanocluster with an Unprecedented Rhombohedral Ag_8 Core. *J. Am. Chem. Soc.* **2020**, *142*, 16905−16909.
(41) Zhao, X.-L.; Wang, Q.-M.; Mak, T. C. W. Self-Assembled Silver Polyhedra with Embedded Acetylide Dianion Stabilized by Perfluorocarboxylate and 4-Hydroxyquinoline Ligands. *Inorg. Chem.* **2003**, *42*, 7872−7876.
(42) Guan, Z. J.; Zeng, J. L.; Nan, Z. A.; Wan, X. K.; Lin, Y. M.; Wang, Q. M. Thiacalix[4]arene: New Protection for Metal Nanoclusters. *Sci. Adv.* **2016**, *2*, No. e1600323.
(43) Bian, S.-D.; Wu, H.-B.; Wang, Q.-M. A Facile Template Approach to High-Nuclearity Silver(I) Alkynyl Clusters. *Angew. Chem., Int. Ed.* **2009**, *48*, 5363−5365.
(44) Jiang, Z.-G.; Shi, K.; Lin, Y.-M.; Wang, Q.-M. $[Ag_{70}(PW_9O_{34})_2(^tBuC{\equiv}C)_{44}(H_2O)_2]^{8+}$: Ionothermal Synthesis of a Silver Cluster Encapsulating Lacunary Polyoxometalate Ions. *Chem. Commun.* **2014**, *50*, 2353−2355.
(45) Zhou, K.; Geng, Y.; Yan, L.-K.; Wang, X.-L.; Liu, X.-C.; Shan, G.-G.; Shao, K.-Z.; Su, Z.-M.; Yu, Y.-N. An Ultrastable $\{Ag_{55}Mo_6\}$ Nanocluster with a Ag-Centered Multishell Structure. *Chem. Commun.* **2014**, *50*, 11934−11937.
(46) Huang, R.-W.; Wei, Y.-S.; Dong, X.-Y.; Wu, X.-H.; Du, C.-X.; Zang, S.-Q.; Mak, T. C. W. Hypersensitive Dual-Function Luminescence Switching of a Silver-Chalcogenolate Cluster-based Metal-Organic Framework. *Nat. Chem.* **2017**, *9*, 689−697.
(47) Rais, D.; Yau, J.; Mingos, D. M. P.; Vilar, R.; White, A. J. P.; Williams, D. J. Anion-Templated Syntheses of Rhombohedral Silver-Alkynyl Cage Compounds. *Angew. Chem., Int. Ed.* **2001**, *40*, 3464−3467.
(48) Schmidbaur, H.; Schier, A. Argentophilic Interactions. *Angew. Chem., Int. Ed.* **2015**, *54*, 746−784.
(49) Yao, Q.; Chen, T.; Yuan, X.; Xie, J. Toward total Synthesis of Thiolate-Protected Metal Nanoclusters. *Acc. Chem. Res.* **2018**, *51*, 1338−1348.
(50) Gupta, A. K.; Orthaber, A. Alkynyl Coinage Metal Clusters and Complexes-Syntheses, Structures, and Strategies. *Chem.—Eur. J.* **2018**, *24*, 7536−7559.
(51) Bowden, T. A.; Milton, H. L.; Slawin, A. M. Z.; Lightfoot, P. Hydrothermal Syntheses and Crystal Structures of Three Zinc Succinates: $Zn(C_4H_4O_4)$-α, $Zn(C_4H_4O_4)$-β and $K_2Zn(C_4H_4O_4)_2$. *Dalton Trans.* **2003**, 936−939.
(52) Ghosh, A. K.; Ghoshal, D.; Zangrando, E.; Ribas, J.; Ray Chaudhuri, N. Syntheses, Crystal Structures, and Magnetic Properties of Metal-Organic Hybrid Materials of Cu(II): Effect of a Long Chain Dicarboxylate Backbone, and Counteranion in Their Structural Diversity. *Inorg. Chem.* **2007**, *46*, 3057−3071.
(53) Yang, G.-P.; Wang, Y.-Y.; Liu, P.; Fu, A.-Y.; Zhang, Y.-N.; Jin, J.-C.; Shi, Q.-Z. Formation of Three New Silver(I) Coordination Polymers Involving 1,2-Phenylenediacetic Acid via the Modulation of Dipyridyl-Containing Ligands. *Cryst. Growth Des.* **2010**, *10*, 1443−1450.
(54) Chen, T.; Fung, V.; Yao, Q.; Luo, Z.; Jiang, D.-e.; Xie, J. Synthesis of Water-Soluble $[Au_{25}(SR)_{18}]^-$ Using a Stoichiometric Amount of $NaBH_4$. *J. Am. Chem. Soc.* **2018**, *140*, 11370−11377.
(55) Yao, Q.; Yuan, X.; Fung, V.; Yu, Y.; Leong, D. T.; Jiang, D. E.; Xie, J. Understanding Seed-Mediated Growth of Gold Nanoclusters at Molecular Level. *Nat. Commun.* **2017**, *8*, 927.
(56) Baksi, A.; Bootharaju, M. S.; Chen, X.; Häkkinen, H.; Pradeep, T. $Ag_{11}(SG)_7$: A New Cluster Identified by Mass Spectrometry and Optical Spectroscopy. *J. Phys. Chem. C* **2014**, *118*, 21722−21729.
(57) Chen, T.; Yao, Q.; Nasaruddin, R. R.; Xie, J. Electrospray Ionization Mass Spectrometry: A Powerful Platform for Noble-Metal Nanocluster Analysis. *Angew. Chem., Int. Ed.* **2019**, *58*, 11967−11977.
(58) Luo, Z.; Nachammai, V.; Zhang, B.; Yan, N.; Leong, D. T.; Jiang, D.-e.; Xie, J. Toward Understanding the Growth Mechanism: Tracing all Stable Intermediate Species from Reduction of Au(I)-Thiolate Complexes to Evolution of Au_{25} Nanoclusters. *J. Am. Chem. Soc.* **2014**, *136*, 10577−10580.
(59) Shi, J.-F.; Chen, Z.-J.; Zhang, L.-J.; Zhou, K.; Ji, J.-Y.; Bi, Y.-F. A One-Dimensional Infinite Silver Alkynyl Assembly $[Ag_8(C{\equiv}C^tBu)_5(CF_3COO)_3(CH_3CN)]_n$: Synthesis, Crystal Structure and Properties. *RSC Adv.* **2020**, *10*, 16045−16049.
(60) Maria Garcia, A.; Giraldo, L.; Carlos Moreno, J. 4-Nitrophenol Adsorption from Solution in Water and Tolueno on Carbonized of Chicken, Bovine and Porcine Bones. *Afinidad* **2013**, *70*, 189−194.
(61) Liu, X.; Dou, X.; Li, X.; Qin, L.; Han, S.; Kang, S.-Z. Preparation of an Ni_5P_4/Ni Porous Composite using a Ni Foam as the Skeleton and its Application in the Treatment of Large-Volume Effluent with a High Concentration of 4-Nitrophenol at Room Temperature. *New J. Chem.* **2019**, *43*, 9673−9679.
(62) Zhao, P. X.; Feng, X. W.; Huang, D. S.; Yang, G. Y.; Astruc, D. Basic Concepts and Recent Advances in Nitrophenol Reduction by Gold- and Other Transition Metal Nanoparticles. *Coord. Chem. Rev.* **2015**, *287*, 114−136.
(63) Wunder, S.; Polzer, F.; Lu, Y.; Mei, Y.; Ballauff, M. Kinetic Analysis of Catalytic Reduction of 4-Nitrophenol by Metallic Nanoparticles Immobilized in Spherical Polyelectrolyte Brushes. *J. Phys. Chem. C* **2010**, *114*, 8814−8820.
(64) Yuan, S.-F.; Guan, Z.-J.; Wang, Q.-M. Identification of the Active Species in Bimetallic Cluster Catalyzed Hydrogenation. *J. Am. Chem. Soc.* **2022**, *144*, 11405−11412.
(65) Wunder, S.; Lu, Y.; Albrecht, M.; Ballauff, M. Catalytic Activity of Faceted Gold Nanoparticles Studied by a Model Reaction: Evidence for Substrate-Induced Surface Restructuring. *ACS Catal.* **2011**, *1*, 908−916.
(66) Guan, Z.-J.; He, R.-L.; Yuan, S.-F.; Li, J.-J.; Hu, F.; Liu, C.-Y.; Wang, Q.-M. Ligand Engineering toward the Trade-Off between Stability and Activity in Cluster Catalysis. *Angew. Chem., Int. Ed.* **2022**, *61*, No. e202116965.
(67) Pozun, Z. D.; Rodenbusch, S. E.; Keller, E.; Tran, K.; Tang, W. J.; Stevenson, K. J.; Henkelman, G. A Systematic Investigation of P-Nitrophenol Reduction by Bimetallic Dendrimer Encapsulated Nanoparticles. *J. Phys. Chem. C* **2013**, *117*, 7598−7604.
(68) Liu, B. P.; Yan, S. H.; Zhang, A. T.; Song, Z. Q.; Sun, Q. X.; Huo, B. B.; Yang, W. R.; Barrow, C. J.; Liu, J. Q. Insight into Catalytic Mechanisms for the Reduction of Nitrophenol via Heterojunctions of Gold Nanoclusters on 2D Boron Nitride Nanosheets. *ChemNanoMat* **2019**, *5*, 784−791.

https://doi.org/10.1021/jacs.3c01119
J. Am. Chem. Soc. 2023, 145, 19523−19532